Book of Tutorials and Abstracts

European
Microbeam Analysis Society

EMAS 2018

13th EMAS Regional Workshop

MICROBEAM ANALYSIS IN THE EARTH SCIENCES

4 - 7 September 2018
University of Bristol, Wills Hall, Bristol, Great Britain

Organised in collaboration with:
Mineralogical Society of Great Britain and Ireland
and
University of Bristol

MACRO-MICRO-NANOSCALE SEM/EDS OF EARTH AND PLANETARY MATERIALS

T. Salge[1,2], J. Spratt[1], S. Russell[3], R. Neumann[4], T. Mohr-Westheide[5,6], A. Greshake[5], W.U. Reimold[7], L. Ferrière[8], M.A. Cox[9] and L. Daly[10]

1 Natural History Museum, Imaging and Analysis Centre
Cromwell Road, London SW7 5BD, Great Britain
2 Bruker Nano GmbH
Am Studio 2D, 12489 Berlin, Germany
3 Natural History Museum, Mineral and Planetary Sciences
Cromwell Road, London SW7 5BD, Great Britain
4 Centro de Tecnologia Mineral – CETEM
Av. Pedro Calmon, 900 - Cidade Universitária, 21941-908 Rio de Janeiro, Brazil
5 Museum für Naturkunde - Leibniz Institute for Evolution and Biodiversity Science
Invalidenstrasse 43, 10115 Berlin, Germany
6 Freie Universität Berlin, Institut für Geologische Wissenschaften
Malteserstrasse 74-100, 12249 Berlin, Germany
7 University of Brasilia, Institute of Geosciences
UnB, 70297-400 Brasilia, Federal District, Brazil
8 Naturhistorisches Museum Wien
Burgring 7, 1010 Vienna, Austria
9 Curtin University, School of Earth and Planetary Sciences
GPO Box U1987, 6845 Perth, WA, Australia
10 University of Glasgow, School of Geographical and Earth Sciences
8NN, University Avenue, Glasgow G12 8QQ, Great Britain
e-mail: t.salge@nhm.ac.uk

Tobias Salge is an electron beam microanalyst at the Imaging and Analysis Centre of the Natural History Museum London. He obtained his PhD for an investigation of the ejecta blanket of the terrestrial Chicxulub impact structure in 2007 at the Museum für Naturkunde Berlin. From 2007 till 2014, he worked for Bruker Nano GmbH as a senior application scientist for energy-dispersive X-ray spectrometry. His main research interest is on meteorite impact processes and applying his expertise in X-ray analysis at the sub-micrometre scale using state-of-the art analytical instruments to earth and planetary sciences.

1. ABSTRACT

Technological developments in scanning electron microscopy (SEM), energy-dispersive X-ray spectrometry (EDS), and modern data processing invite novel analytical approaches. We will provide first a brief overview of the various electron sources for SEM and the recent developments in EDS detectors. Standards-based quantification will be presented for silicate analyses. Improved element and mineral identification by hyperspectral imaging techniques is demonstrated for a polymetallic iron ore sample. Automated stage control allows high resolution datasets to be acquired over relatively large areas. High resolution, macro-scale analysis will be presented for the anorthositic lunar meteorite Dhofar081. Mineral classification in relatively large areas by automated feature analysis significantly reduces measurement and evaluation time and has, for example, allowed the identification of extraterrestrial carrier phases in Archean impact spherule deposits of the ICDP BARB5 drill core from South Africa. The possibilities of analysis of low to intermediate X-ray lines with a spatial resolution of <100 nm will be highlighted. A novel methodology – non-destructive, non-invasive X-ray analysis using ultra-low beam current under high vacuum with an annular silicon drift detector – will be demonstrated for the historic meteorite fall Mocs and a grain from the Hayabusa Japan Aerospace Exploration Agency sample-return mission to asteroid 25143 Itokawa.

2. ADVANCES IN SEM AND EDS

The first commercial scanning electron microscopes (SEMs) were built in the early 1960s. Table 1 and Fig. 1 compare the various electron sources used for SEM. Low-cost tungsten (W) filaments are commonly applied and provide a decent performance for conventional SEM analysis at intermediate to high accelerating voltage. Lanthanum hexaboride (LaB_6) cathodes can be used in conventional SEMs by upgrading the vacuum system. They provide a higher emission current density and slightly better resolution than a W filament, but at a comparatively higher cost. The hot Schottky field emission (FE) electron gun uses an orientated tungsten crystal with a zirconium oxide coating that helps to increase electrical conductivity. It combines a higher resolution than W and LaB_6 emitters of ~1 - 5 nm, a good probe current stability and high emission current, which is advantageous for microanalysis at low accelerating voltages. The cold-cathode field emission (CCFE) electron gun uses a single-crystal tungsten emitter and provides the best resolution of up to 0.4 nm.

The first commercial energy-dispersive X-ray spectrometry (EDS) systems appeared in the late 1960s and used the lithium-drifted silicon Si(Li) detector [1]. The Si(Li) detector must be operated at low temperature and was cooled by liquid nitrogen. The silicon drift detector (SDD) [1] was introduced in 1997 and has now become the industry standard. The functional principle of the SDD is shown in Fig. 2a. The SDD consists of a small central anode, which is surrounded by a concentric structure of rings. These are set to successively changing voltages that introduce an

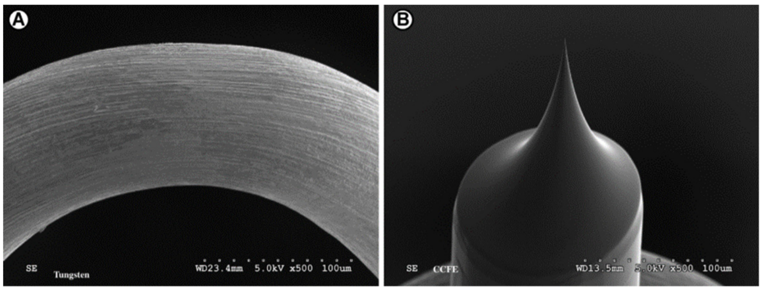

Figure 1. Secondary electron micrographs of electron emitters. a) Tungsten (W) emitter. b) Cold-cathode field emission gun (CCFE, 4,000 hours operating life). Image courtesy: M.J. Grimson, The Imaging Center, Texas Tech University, U.S.A.

Table 1. Comparison of electron sources for scanning electron microscopes.

	Tungsten (W)	Lanthanum hexaboride (LaB_6)	Hot Schottky field emission (FE)	Cold-cathode field emission (CCFE)
Operating Vacuum (Pa)	10^{-2} - 10^{-4}	10^{-4} - 10^{-6}	10^{-7} - 10^{-9}	10^{-4} - 10^{-6}
Emission current density (A/cm^2)	10^4	10^5	5 x 10^6 - 10^7	2 x10^7
Typical probe current (nA)	1,000	1,000	20 – 300	0.2
Tip radius (nm)	60,000	1,000	<1,000	<100
Current stability (%/min)	0.1 - 1.0	0.2 - 2.0	<1.0	4 - 6
Spot size (nm)	3.0	2.0	1.0 - 2.0	0.4 - 1.0
Operating life (h)	100 - 200	600 - 1,000	4,000	5,000

electrical field which creates a central bias at the anode. An X-ray quantum of energy, absorbed in the volume of the detector, causes a cloud of electrons and holes. The electrical field forces the electrons to move towards the anode. A small anode and an integrated field effect transistor (FET) reduce the capacitance. This improves the signal to noise ratio. As the remaining noise is almost independent of the temperature, a SDDs does not need to be cooled with liquid nitrogen. A near room-temperature operation at approximately -20 ºC can be achieved with a Peltier element. The improved signal to noise ratio leads to the ability to process count rates that are 10 times higher than those of typical Si(Li) detectors. Peak shift and peak broadening with increasing count rate are not observed.

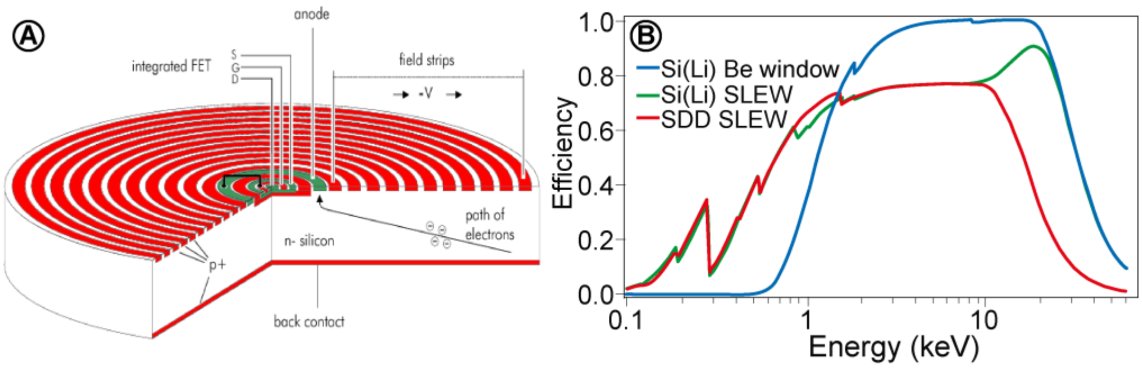

Figure 2. a) Diagram of SDD showing rings to shape the field, small central anode, and on-chip FET (diagram courtesy of PNSensor). b) Plot showing efficiency versus logarithmic X-ray energy for Si(Li)- and SD-detectors with both Be window and Super Light Element Window [1].

The active detector semiconductor chip of a conventional EDS detector is kept under high vacuum and isolated from the chamber of the microscope by a window. In older systems these windows were composed of a 7.5 µm thick beryllium sheet which has a low transmission efficiency for low energy X-rays (Fig. 2b) and allow the user to analyse elements with an atomic number Z ≥ 11 (sodium). Modern systems use a < 0.25 µm polymer window which has a high efficiency for low energy X-rays and allows the analysis of low energy X-ray lines as well.

Conventional EDS detectors have an inclined geometry with a take-off angle between 30° and 35° (Fig. 3). The more recently introduced annular SDD [1-3] is placed between the pole piece and sample and has a 10 - 100 times higher collection efficiency than conventional SDDs. The collection of X-rays from four different directions allows data collection across samples with substantial surface topography.

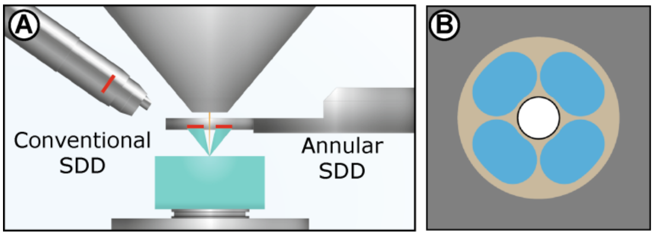

Figure 3. a) Geometry of conventional and annular SDDs. b) Layout of the annular SDD showing four detection segments.

3. SEM IMAGING

Electrons in the primary beam can interact with atoms in the specimen, which can be used to gain information through spectroscopy. These interactions can be divided into elastic and inelastic scattering of electrons. Elastic scattering refers to a change in trajectory without loss of energy. Backscattering of electrons, for example, is such an event. Inelastic scattering refers to a loss of energy of the electron with little change of direction. The production of secondary electrons (SE) and X-rays are such events. The signals produced by these processes can be used for imaging. Low energy (50 eV) SE only escape from within a very shallow zone at the surface of the sample. Detection of SE by the Everhardt-Thornley detector allows the surface shape (topography) to be imaged. The number of backscattered electrons (BSE) depends on the composition of the sample; detection of BSE by a solid-state silicon semiconductor provides information of the material contrast.

Non-conductive samples are usually coated with a thin conductive layer of heavy elements or carbon to inhibit charging. Gold or palladium is used to improve the SE signal for topographic imaging. Carbon coating is preferred for X-ray analysis, due to its low density, reduced X-ray absorption, and small number of X-ray emission lines. Precious samples, which do not allow coating, can be analysed using a variable pressure (VP) SEM at higher chamber pressures (~10 Pa to 400 Pa). The collisions of the electron beam with gas molecules produce positive ions that migrate to negatively charged areas of the specimen and neutralise the surface charge (Fig. 4). For X-ray microanalysis in VP mode, gas scattering leads to direct contributions to the spectrum from the environmental gas, as well as remote generation of X-rays by electrons scattered out of the focussed beam [4]. This so-called beam skirting significantly reduces the spatial resolution for X-ray microanalysis (Fig. 5). Alternatively, imaging can be performed under high vacuum using low accelerating voltage. The necessity here, of low probe currents would give low X-ray count rates with conventional EDS detectors, which, however, can be improved by using multiple detectors or an annular SDD.

4. ADVANCING EDS MICROANALYSIS

4.1. EDS quantification

Quantitative analysis includes four steps: (1) element identification, (2) background removal, (3) peak deconvolution, and (4) quantification. Standardless analysis provides satisfactory results for many applications. The standardless results, however, need to be normalised to a total of 100 mass% which leads to errors for water bearing minerals. The un-normalised totals of standards-based results are an indicator of the accuracy whereby 100 ± 2 mass% is normally the accepted range. When performing standards-based analysis, the following is relevant: Samples must be polished to avoid absorption effects, aligned perpendicular to the electron beam, and

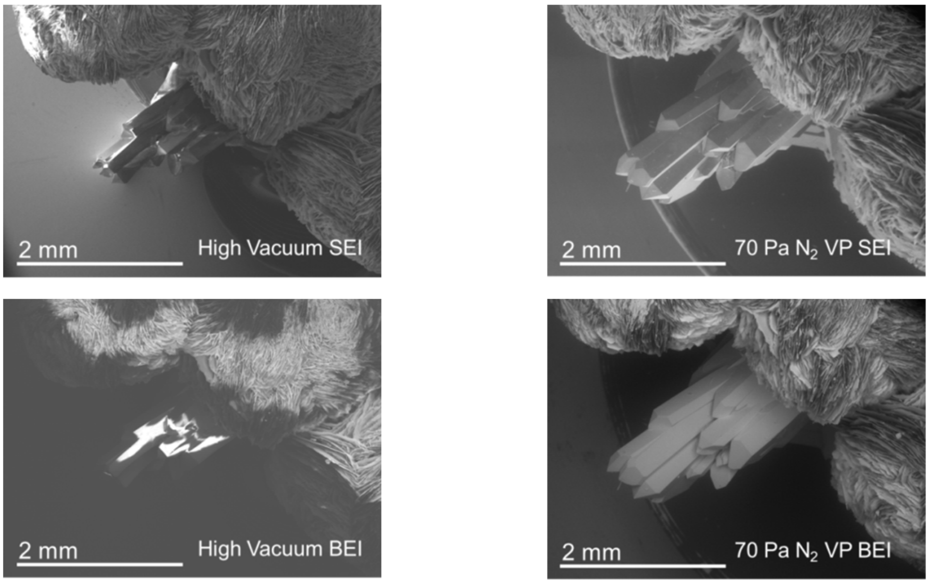

Figure 4. Comparison of SE imaging (SEI) and BSE imaging (BEI) at high vacuum and variable pressure mode of an uncoated, non-conductive sample (quartz and zeolite).

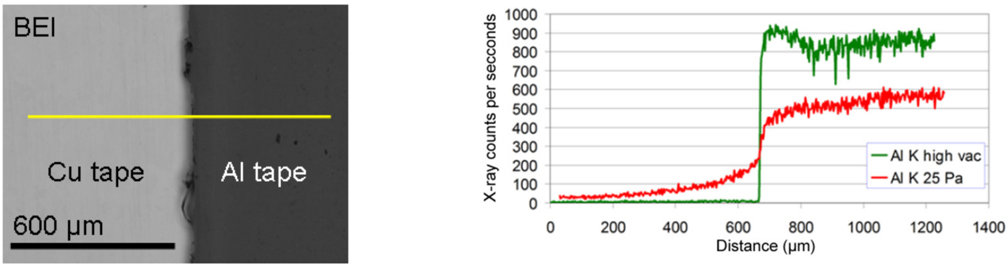

Figure 5. Line-scans of a copper, aluminium interface acquired at high vacuum (10^{-2} - 10^{-4} Pa) and at low vacuum (25 Pa). At low vacuum, contribution from aluminium can be observed at copper over a distance of several 100 s of µm (20 kV, 1.48 nA, 80 mm^2 SDD, W-SEM).

non-conductive samples must be carbon coated. Unknowns and standards must be analysed on the same instrument and under the same operating conditions. As the beam current has a direct influence on the analysis total, it must be monitored either directly with a Faraday cup, or indirectly by measuring a reference sample e.g. cobalt. Conventional SEMs with tungsten filaments may reach a stable beam current after ~60 minutes (Fig. 6). A dedicated vacuum pump for the electron gun can improve the beam stability specifically after a sample change and may extend the filament operating life to 1000s of hours.

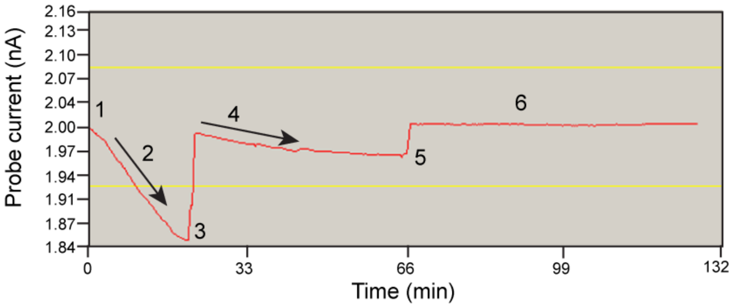

Figure 6. Diagram showing probe current changes during adjustment of the electron beam to achieve stability. (1) Turning filament and accelerating voltage on. (2) Beam current quickly drops. (3) Beam alignment using the shift and tilt coils. (4) Beam current slowly drops. (5) Beam alignment using the shift and tilt coils. (6) Beam stabilisation.

The minimum detection limit for routine EDS analysis depends on the impulse statistics. This is generally taken to be the peak height equal to three times the standard deviation of the background count. Better impulse statistics improve the peak to background ratio and lower the detection limit. A detection limit below 0.1 mass% can be achieved (Fig. 7). Table 2 compares EDS quantification results at different impulse statistics with additional wavelength-dispersive X-ray spectrometry (WDS) results. For elements with concentrations near the detection limit of ~0.1 mass%, better impulse statistics result in a lower standard deviation of mean values and improved precision. The results presented were obtained from a four year old calibration and document that standards-based EDS quantification can achieve precise and accurate results. For elements with low concentration and significant peak overlaps in EDS spectra, however, WDS can obtain better results due to its better spectral resolution and superior signal to noise ratio.

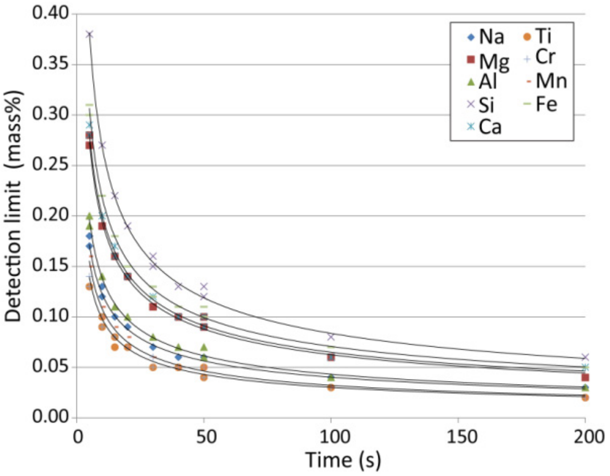

Figure 7. Detection limits of elements for reference material NMNH 122142 Augite, Kakanui, New Zealand versus life time (20 kV, 3 nA, ~12 kcps, 80 mm^2 SDD, W-SEM).

Table 2. Reference material NMNH 122142 Augite, Kakanui, New Zealand. Comparison of standards-based results (mass%) at different impulse statistics (50 k, 250 k and 1,000 k impulses at 0.35 - 20 keV) to WDS results. Oxygen was quantified by stoichiometric calculation, Fe is presented as FeO. (20 kV, 3 nA, ~12 kcps, 80 mm^2 SDD, W-SEM). Values in brackets for Cr and Mn at 50 k are below detection limit.

	n	Na	Mg	Al	Si	Ca	Ti	Cr	Mn	Fe	O	Total
Provided[1]		0.94	10.0	4.16	23.7	11.3	0.44	n.a.	0.10	5.26	44.0	100.4
Provided[2]		0.94	10.0	4.62	23.7	11.3	0.44	n.a.	0.10	4.93	44.5	100.5
WDS	21	1.01	9.88	4.17	23.7	11.5	0.51	0.11	0.11	4.91	44.0	99.9
s (± mass%)		0.02	0.07	0.07	0.06	0.07	0.01	0.01	0.01	0.03	0.11	
EDS 50 k	12	0.92	9.93	4.29	23.5	11.8	0.58	(0.17)	(0.12)	4.89	44.1	100.3
s (± mass%)		0.10	0.20	0.14	0.30	0.29	0.10	0.07	0.09	0.29	0.41	
EDS 250 k	12	0.93	9.84	4.36	23.6	11.7	0.54	0.15	0.08	4.95	44.1	100.2
s (± mass%)		0.06	0.08	0.05	0.12	0.1	0.05	0.04	0.05	0.09	0.21	
EDS 1000 k	12	0.89	9.89	4.21	23.5	11.6	0.50	0.17	0.09	4.99	43.8	99.6
s (± mass%)		0.04	0.04	0.03	0.07	0.05	0.02	0.02	0.03	0.04	0.15	

[1] Values of [5]. [2] Preferred values of [6]. n.a.: not analysed.

Table 3. Inter-laboratory EDS test glass sample (NanoAnalytics GmbH, LV16). Comparison of standards-based quantification results (mass%) showing the influence of spectrum acquisition from areas (~40 x 40 µm) versus points, and live time. Values given in bold font represent results that differ due to the effect of sodium migration. Measurement conditions as in Table 2.

Spectrum	n	Na	Mg	Al	Si	S	K	Ca	Fe	O	Total
Area 20 s	11	10.3	2.37	0.71	33.9	0.10	0.55	5.36	0.17	46.9	100.3
s (± mass%)		0.08	0.06	0.04	0.21	0.04	0.04	0.11	0.06	0.26	0.53
Area 200 s	11	10.3	2.39	0.72	34.0	0.09	0.56	5.34	0.19	46.9	100.4
s (± mass%)		0.04	0.03	0.01	0.07	0.004	0.02	0.03	0.02	0.10	0.21
Point 20 s	11	**8.7**	2.36	0.73	34.0	0.09	0.55	5.37	0.20	46.4	**98.3**
s (± mass%)		0.20	0.06	0.03	0.17	0.04	0.04	0.09	0.06	0.29	0.68
Point 200 s	11	**3.4**	2.43	0.74	**35.5**	0.10	**0.47**	5.50	0.21	46.4	**94.7**
s (± mass%)		0.04	0.02	0.02	0.12	0.01	0.02	0.04	0.01	0.18	0.39
EDS test	85	10.1	2.4	n.d.	33.9	n.d.	n.d.	5.4	n.d.	46.7	

n.d.: not determined by a significant proportion of the 85 inter-laboratory test participants.

Alkali ions, especially sodium and potassium migrate away from the point of beam impact during routine X-ray analysis of glasses. Table 3 shows results of a sodium-rich glass sample from an inter-laboratory test sample provided by nanoAnalytics GmbH. Spectrum acquisitions of points reveal significantly lower sodium (and potassium) concentrations with time, and increased concentrations for other elements (e.g., silicon). The acquisition of 40 x 40 µm area spectra can compensate this effect.

4.2. Hyperspectral imaging

For hyperspectral imaging [1] it is essential to adjust the pixel size, which depends on the map resolution and magnification, to the spatial resolution for emitted X-rays. The resolution can be estimated by performing Monte Carlo simulations and depends on the density and the accelerating voltage. For conventional microanalysis with 20 kV, the spatial resolution is in the micrometre-range and can be improved to the sub-micrometre scale using a low accelerating voltages (Fig. 8).

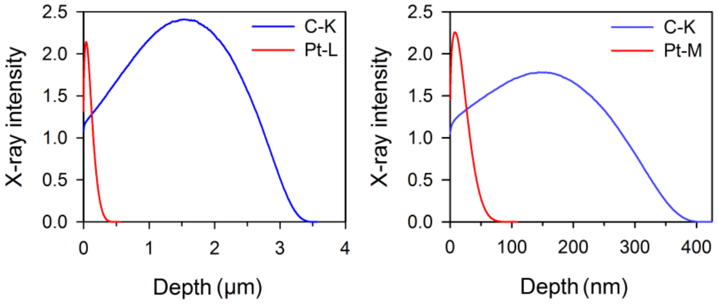

Figure 8. X-ray excitation depth functions showing the intensity of X-ray lines for pure carbon and pure platinum at 20 kV (left) and 6 kV (right). At 6 kV, the highest intensities are emitted from a depth of ~20 nm for Pt-M and ~200 nm for C-K.

Hyperspectral imaging datasets provide complete spectra for each pixel of the SEM micrograph and permit data mining. Figure 9 shows results from a polymetallic iron ore [7]. The low energy performance of modern EDS systems allows hematite to be distinguished from magnetite by intensity maps of oxygen and iron (Fig. 9b). Similarly, composed spectra can be detected by chemical phase mapping with the help of mathematical methods (principal component or cluster analysis) or user defined areas. The result (Fig. 9c) with consideration of oxygen, iron and silicon concentrations allows the identification of magnetite and hematite.

Element identification can be improved by using the Maximum Pixel Spectrum function [8]. This function synthesises a spectrum consisting of the highest count level found in each spectrum energy channel. Even elements that occur in only a few or just one pixel of an element map can be easily identified. Some elements, in this example had not been targeted by conventional wet-chemical analysis, but were identified by the Maximum Pixel Spectrum function (Fig. 9d), extracted pixel

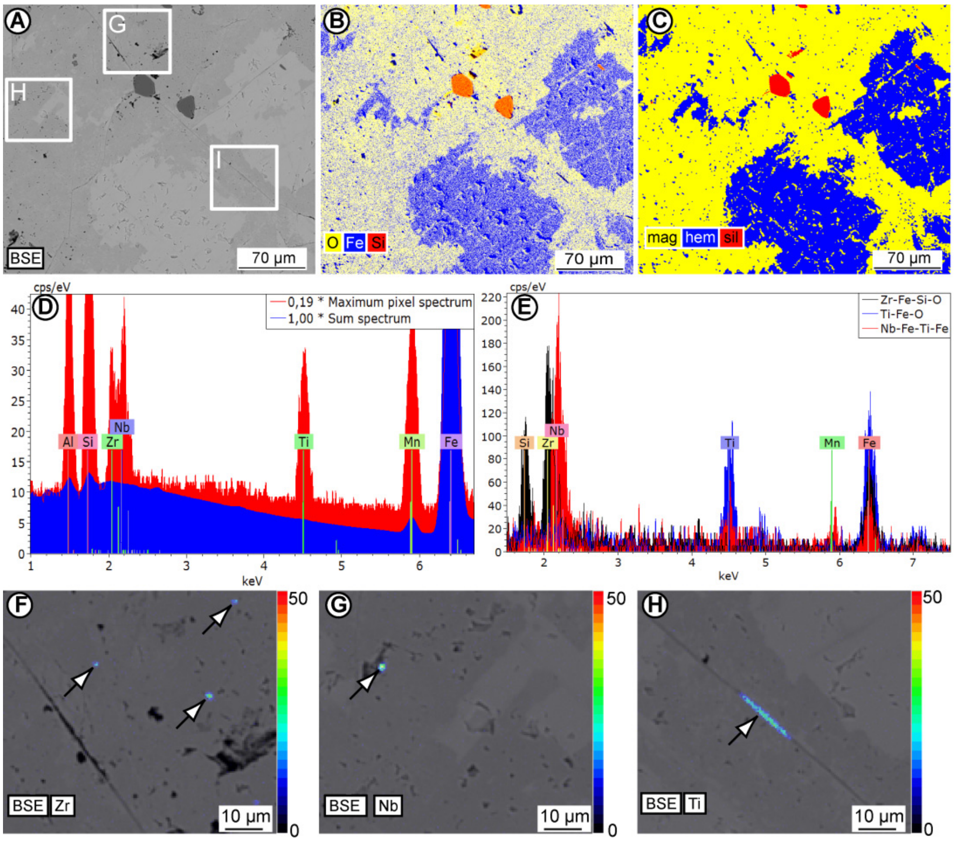

Figure 9. Polymetallic iron ore [7]. a) BSE micrograph of the area analysed by hyperspectral imaging, rectangles show magnified areas in (F to H). b) Composite intensity map of oxygen, iron and silicon. c) Result of chemical phase analysis showing the distribution of magnetite (mag, 65.5 % area fraction), hematite (hem, 33.5 % area fraction) and silicates (sil, 1 % area fraction). d) Comparison of the sum spectrum (blue) of the analysed area and the Maximum Pixel Spectrum (red). Elements present in only a few pixels of the map cannot be displayed in the sum spectrum due to the low overall concentration but are clearly identifiable in the Maximum Pixel Spectrum. e) Spectra extracted from a single pixel of the map (~2,000 counts in the complete spectrum). F to h) Magnified quantitative maps (mass%) of the areas shown in (a). 15 kV, 220 kcps, 700 x 604 pixels, 0.47 µm pixel size, 2h12 min, 30 mm^2 SDD, FE-SEM.

spectra (Fig. 9e), and quantitative mapping (Figs. 9f-h). Zirconium is associated to silicon, due to small zircon inclusions. Niobium points to small Fe(Mn) columbite inclusions. Titanium-rich inclusions have also been identified, and could be related to fractures in the ore.

4.3. High resolution imaging at the macroscale

Using automatic motorised stage control, it is possible to acquire several datasets over a larger area. Then 64-bit processing by modern computer systems allows montaging of the individual datasets to one file at high pixel resolution. Figure 10a shows a 22 megapixel (MP) mosaic from 480 individual fields of the complete sample of a lunar meteorite covering an area of 14.6 x 6.0 mm. Acquisition at an accelerating voltage of 20 kV allows the maps to be acquired at a pixel resolution of 2 µm. A smaller area was analysed at an accelerating voltage of 10 kV and 0.5 µm pixel resolution (Figs. 10b and 10c). The 21 MP mosaic from 28 fields provides insight into the formation of the fine-grained, heterogeneous matrix.

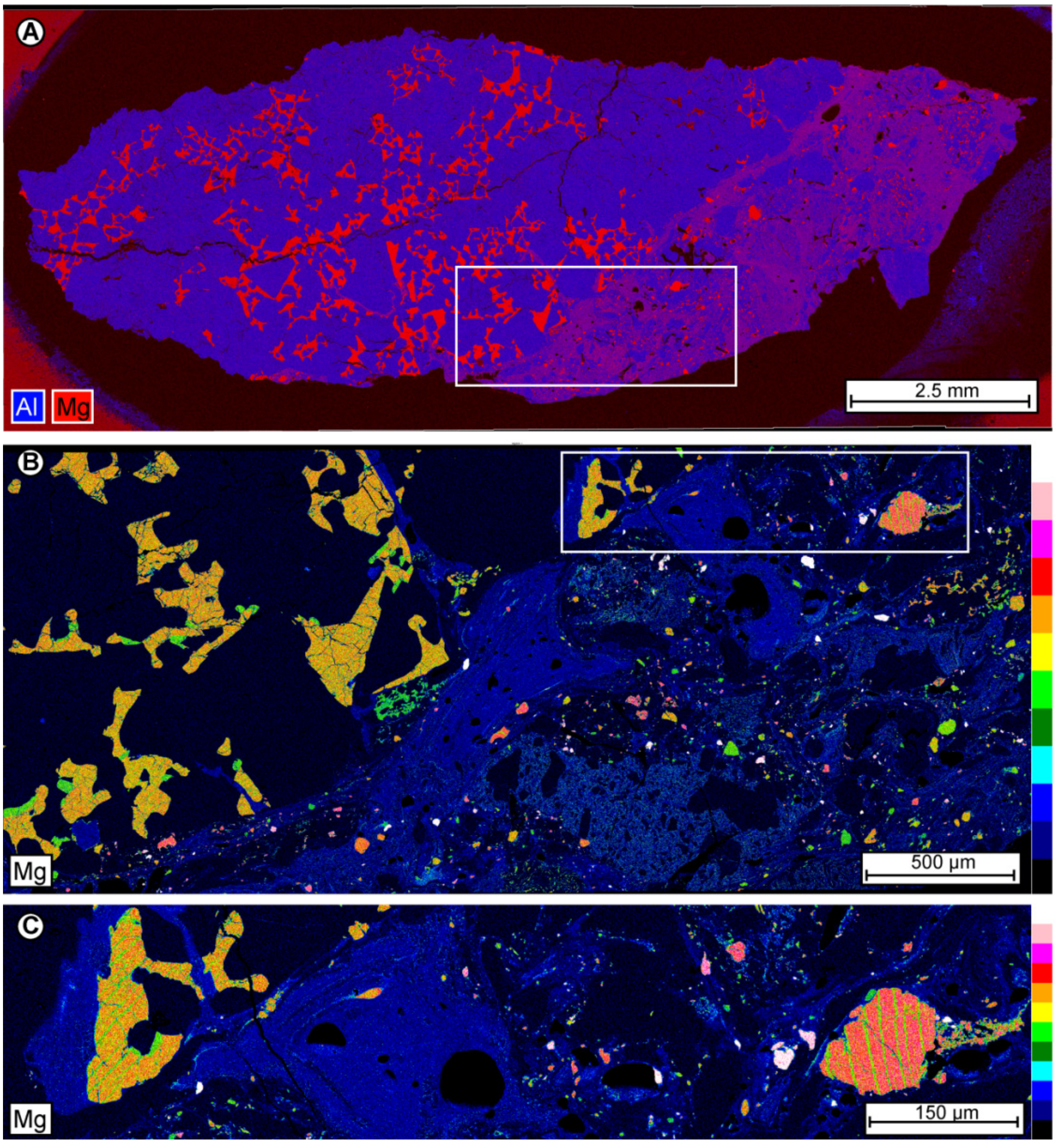

Figure 10. High resolution mosaic maps of anorthositic lunar meteorite Dhofar081 (BM.2004,M5, P12267). a) Composite map of the complete sample showing a fine-grained, heterogeneous matrix at the right sample area. 20 kV, 6.6 nA, 113 kcps, 7295 x 2986 pixels, 2 µm size, 33 h, 80 mm^2 SDD, FE-SEM. b) Magnesium in false colour display of the white rectangle shown in (a). 10 kV, 4.5 nA, 53 kcps, 6851 x 3058 pixels, 0.5 µm pixel size, 4 h. c) Image detail of the white rectangle in (b).

4.4. Automated feature analysis

Minerals in large analysis areas can be classified by automated feature analysis with stage control, a combination of morphological classification by image analysis and chemical analysis. Analysing only features of interest by selecting the corresponding threshold in the BSE micrograph significantly reduces measurement and evaluation time. The following example describes a method to identify the extraterrestrial component carrier phases in a sample of Archean impact spherule layers [9].

Figure 11a shows impact spherule layers in a section from the ICDP BARB5 drill core, from the Barberton Mountain Land, South Africa. Ni-rich chromium spinel clusters are associated with PGE-rich metal alloy and PGE sulpharsenide grains of 0.6 to 1.4 µm diameter (measurement conditions are mentioned in Table 4). A larger area (Fig. 11a, red rectangle) was analysed with a BSE pixel resolution of 2 µm using 20 kV. Ni-Cr spinel grains with a circle radius > 6 µm were classified by their elevated nickel concentrations (Figs. 11b-e). For the classification of PGE phases (Fig. 11f), the spatial resolution was enhanced to the sub-micrometre scale by using an accelerating voltage of 6 kV. A smaller region (Fig. 11a, blue rectangle) was analysed with a BSE pixel resolution of 100 nm in order to identify grains with a maximum circle radius > 250 nm. Plotting the stage coordinates of Ni-Cr spinels and PGE phases (Fig. 11g) shows the association of both phases with each other.

Table 4. Measurement conditions for feature analysis of Ni-Cr spinel and PGE phases.

	Ni-Cr spinel	**PGE**
BSE threshold	Intermediate to bright	bright
Pixel resolution	~2 µm	~100 nm
Accepted particles	6 µm radius	250 nm radius
Spectrum acquisition	Full particle (2 µm scan guard band)	Particle centre
HV	20 kV	6 kV
Input count rate	~90 kcps	~70 kcps
Spectrum acquisition time	0.5 s	3 s
Fields	288 (400x266 pixels)	170 (3,600x2,397 pixels)
BSE acquisition time per field	0.9 s (8 µs dwell time)	17 s (2 µs dwell time)
Analysed area	495,613 µm^2	89,746 µm^2
Particle count	707 (~200 Ni-Cr spinel)	38 (17 PGE phases)
Total time	60 min	90 min

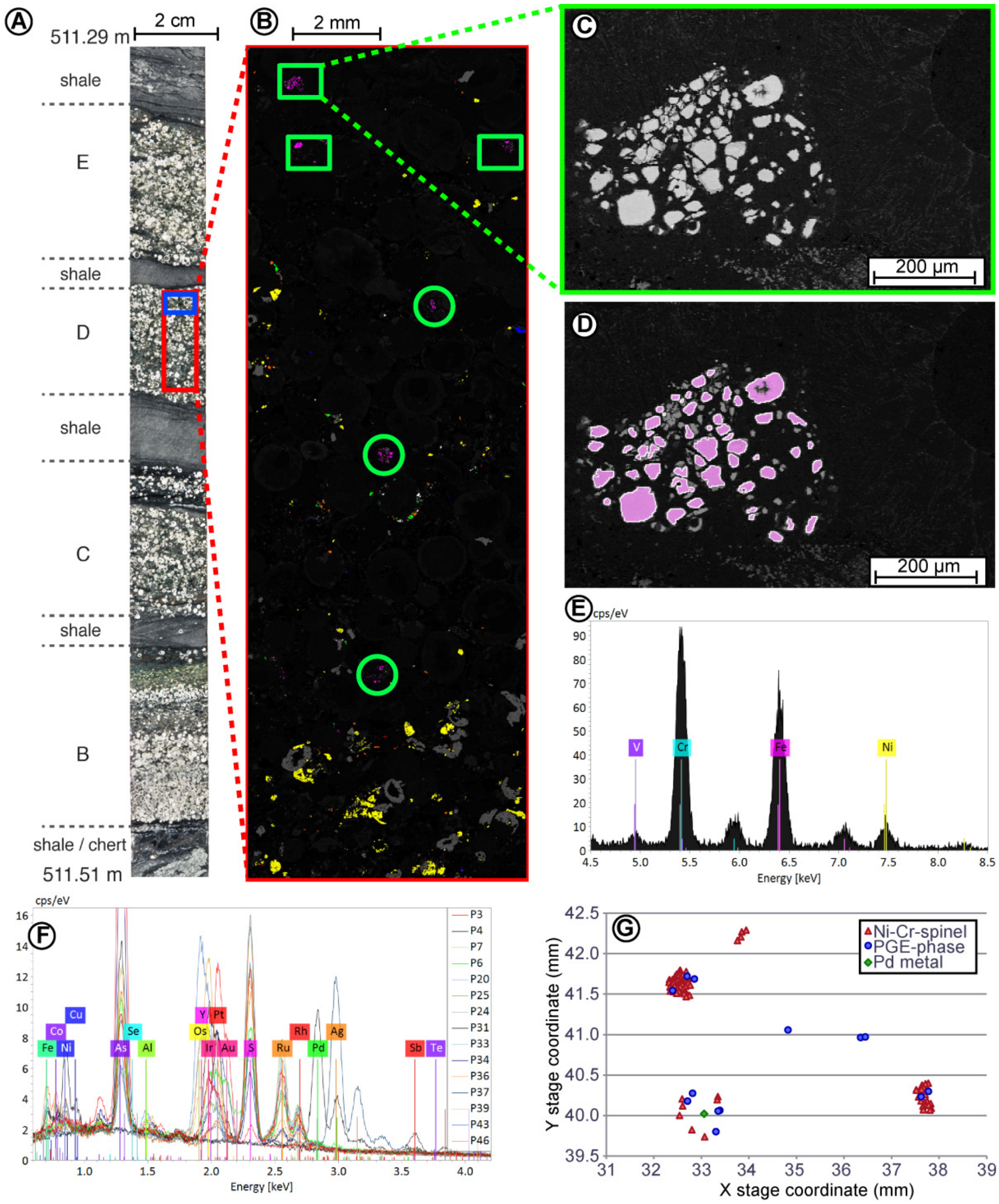

Figure 11. Feature analysis of Ni-Cr spinel and platinum group element (PGE) phases in ICDP BARB5 drill core (10 mm^2 SDD, FE-SEM). a) Photograph of the drill core sample showing impact spherule layers and regions, which were analysed to identify Ni-Cr spinel (red rectangle) and PGE phases (blue rectangle), image modified after [9]. b) Feature analysis result of the complete analysed area overlaid onto BSE micrograph. Green outlined areas show identified Ni-Cr spinel clusters. c and d) BSE micrograph and feature analysis result for one field showing a Ni-Cr spinel cluster. e) Automatically acquired spectrum of a Ni-Cr spinel grain showing elevated Ni intensities. f) Spectra of classified PGE phases (0.6 - 1.4 µm diameter, see Fig. 12). g) Diagram showing SEM stage coordinates of classified grains, modified after [9].

4.5. *Low voltage EDS analysis*

The distribution of elements with overlapping X-ray peaks can be displayed with a spatial resolution < 100 nm by net intensity maps using background subtraction and peak deconvolution (Fig. 12). Sample drift that may be significant at high magnifications can be compensated by drift correction options. As the emitted X-rays derive from a low depth, the contamination of hydrocarbons during any acquisitions lowers the intensities of X-rays from other elements (arrows in Figs. 12d and 12e). The quantification of X-ray lines < 1 keV is challenging [10], due to: absorption edges within the Bremsstrahlung background, the energy dependence of efficiency, and uncertainties of absorption effects. Preliminary results on PGE metal nuggets indicate that EDS deconvolution algorithms allow the quantification of the L- and M-line families of Ru, Rh, Pd, Re, Os, Ir, Pt at ~2 - 3 keV with totals close to 100 mass% [11].

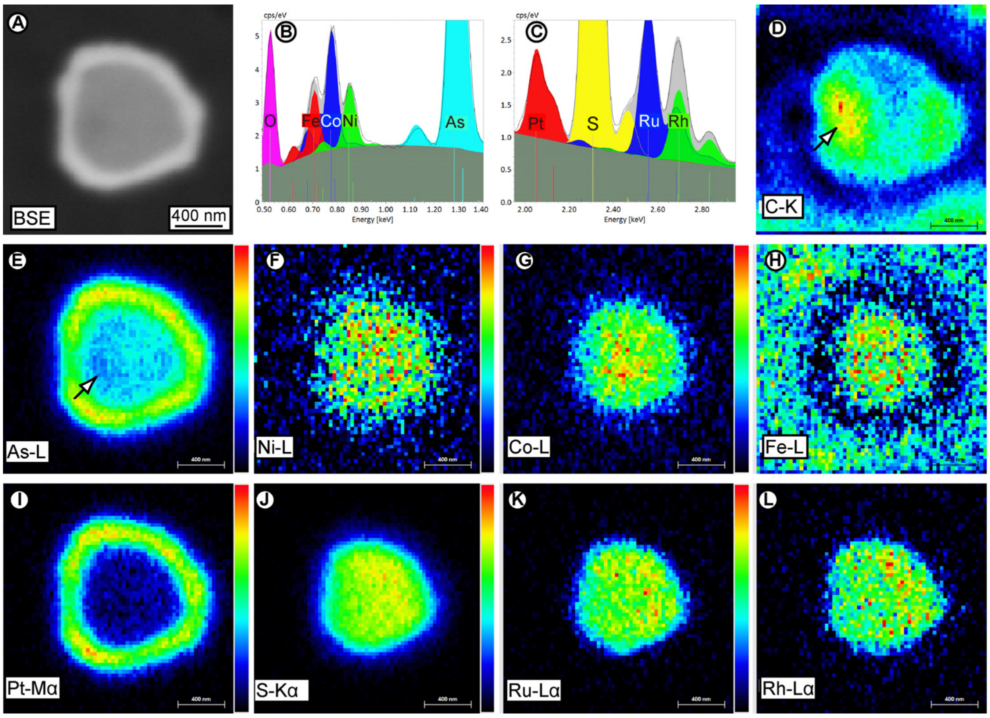

Figure 12. Low voltage analysis of a PGE-sulpharsenide grain from a sample of the ICDP BARB5 drill core. a) BSE micrograph. b and c) Deconvolution result of energy lines in the low (0.5 - 1.4 keV) and intermediate (1.95 - 2.95 keV) energy range. d to l) Net intensity maps (6 kV, 52 min, 8 kcps, 30.6 nm pixels, 10 mm^2 SDD, FE-SEM).

4.6. *Non-destructive, non-invasive EDS at high vacuum*

The high collection efficiency of the annular SDD allows data collection on uncoated, non-conductive samples with substantial surface topography using ultra low beam currents under high vacuum. A map of the historic Mocs L5-6 meteorite (Fig. 13a) acquired at 6 kV and ~10 pA reveals that lead from historical polishing processes and soot from heating with coal-fired furnaces was deposited onto the sample surface that may consist of sulphide and oxide minerals [3]. The overlapping Pb-M and S-K peaks (Fig. 13b) were automatically deconvoluted. The map of a smaller region (Fig. 13c) demonstrates that carbon features < 300 nm in size can be displayed under high-vacuum conditions using low accelerating voltage and ultra-low probe current.

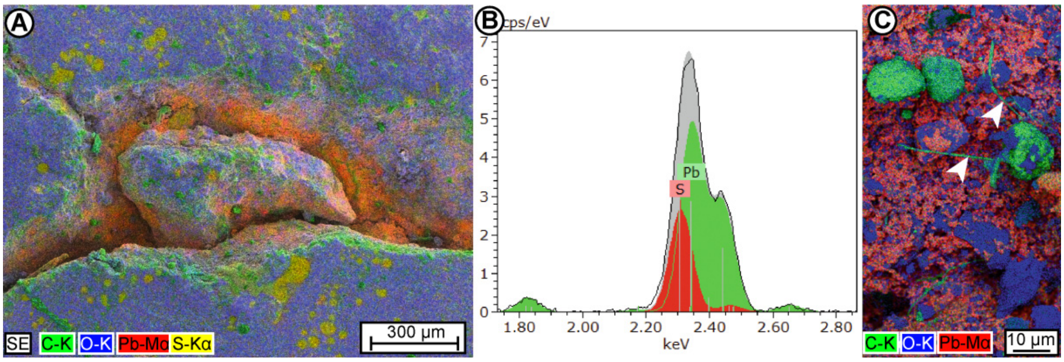

Figure 13. Mocs historic meteorite NHMW-H9898. a) Composite map overlaid onto SE micrograph (6 kV, 10 pA, 2.9 kcps, 800 x 600 pixels, 2 µm pixel size, 47 min, annular SDD, FE-SEM). b) Deconvolution result showing the separation of the overlapping Pb-M and S-K peaks. c) Composite map (6 kV, 10 pA, 2.4 kcps, 412 x 732 pixels, 130 nm pixel size, 5h10 min) showing carbon filaments < 300 nm in size. Copyright: [3], © Microscopy Society of America 2017, published by Cambridge University Press.

The second example for non-invasive sample analysis is related to JAXA's Hayabusa mission to asteroid 25143 Itokawa, which returned approximately 1,500 grains [12]. Some previous studies involved mounting a single grain in epoxy followed by polishing to obtain a flat surface, e.g., [13]. This results in the loss of up to 50 % of this precious material and risks losing these tiny grains due to 'plucking' during polishing. The analysed particle RB-CV-0087 is a complex multiphase particle previously described as containing low calcium pyroxene, iron sulphide and FeNi metal phases. EDS analysis at 6 kV and 25 pA (Fig. 14) reveals that, in addition, it also contains olivine and feldspar, and some of the FeNi metal is replaced by sulphide. Phase boundaries are readily observable and recognisable as the surface expression of twinning in pyroxene.

5. *CONLUSIONS*

Technological developments in SEM/EDS and modern data processing set the stage for hyperspectral imaging techniques that can enhance the identification of elements and minerals. Large area mapping at high spatial, high pixel resolution permits the study of small-scale processes. The classification of specific minerals in large analysis areas is possible over short measurement times by feature analysis. Using low accelerating voltages, the spatial resolution for X-ray microanalysis can be enhanced to the sub-micrometre scale. FE-SEM/EDS at low beam current

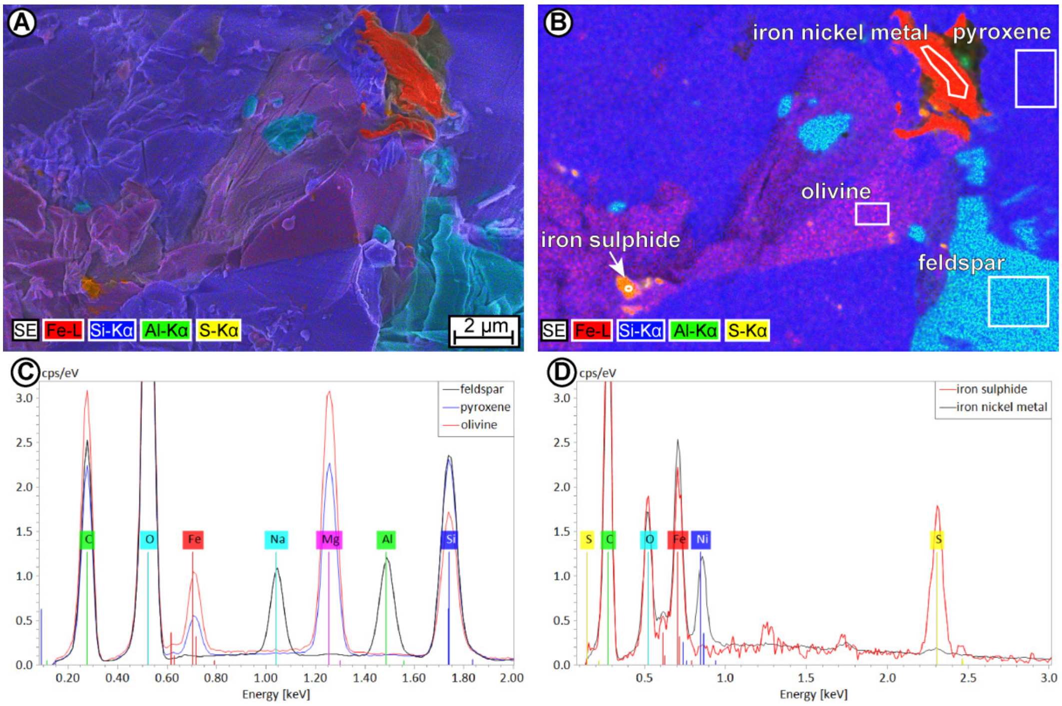

Figure 14. Itokawa particle RB-CV-0087 from JAXA's Hayabusa sample return mission. a) Composite map overlaid onto SE micrograph. b) Composite map showing rectangles where spectra were extracted from the hyperspectral imaging dataset. C and d) Area spectra showing the presence of sodium-rich feldspar, pyroxene, olivine, iron nickel metal and iron sulphide. (6 kV, 25 pA, 3 kcps, 1200 x 800 pixels, 15 nm pixel size, 14 h, annular SDD, FE-SEM).

with an annular SDD provides high spatial resolution and high detection sensitivity without the necessity of applying a conductive coating or working in low vacuum. Compared to low vacuum analysis, this approach avoids beam skirting effects. In addition, hydrocarbon contamination is reduced. The possibility to analyse beam sensitive or precious specimens in a close to natural state with little preparation and to study fine scale structures and surface layers will stimulate new approaches for earth and planetary sciences and allows to target specific regions for further investigations with, e.g., transmission electron microscopy, atom probe microscopy and nanoscale secondary ion mass spectrometry.

6. *REFERENCES*

[1] Friel J J, Terborg R, Langner S, Salge T, Rohde M and Berlin J 2017 *X-ray and image analysis in electron microscopy*, 3rd ed. (Berlin: Pro Business)
[2] Hodoroaba V D, *et al.* 2016 *IOP Conf. Ser.: Mat. Sci. Engng* **109** 012006
[3] Terborg R, *et al.* 2017 *Microscopy Today* **25** 30-35
[4] Newbury D E 2002 *J. Res. Natl. Inst. Stand.* **107** 605-617
[5] Jarosewich E, Nelen J A and Norberg J A 1980 *Geostandard. Newslett.* **4** 43-47

[6] https://mineralsciences.si.edu/facilities/standards/datasheets/AugiteKakanui_NMNH-122142.pdf
[7] Salge T, *et al.* 2013 *23rd IMCET* 357-367
[8] Bright D S and Newbury D E 2004 *J. Microscopy* **216** 186-193
[9] Mohr-Westheide T, *et al.* 2015 *Geology* **4** 299-302
[10] Llovet X, *et al* 2012 *IOP Conf. Ser.: Mat. Sci. Engng.* **32** 012014
[11] Salge T, Krzesinska A and Mohr-Westheide T 2017 *Meteorit. Planet. Sci.* **52** 6209
[12] Nakamura T, *et al.* 2011 *Science* **333** 1113-1116
[13] Jourdan F, *et al.* 2017 *Geology* **45** 819-822